HiLL PUBLISHING

OAJRC Material Science, 2025, 7(2), 24-33
https://www.hillpublisher.com/journals/oajrcms/
ISSN Online: 2632-2072

# Mg-doped $Al_2O_3$ Nanoparticles: Synthesis, Structural, and Optical Studies Prepared Through Mechanical Ball Milling

**Nakka Praveenkumar[1], Michael Hlongwane[1], Peter M. Norton[1], Wendy B. Mdlalose[1], Thishana Singh[2], Mathew K. Moodley[1,*]**

[1]Discipline of Physics, University of KwaZulu-Natal, Westville Campus, Durban 4000, South Africa.
[2]Discipline of Chemistry, University of KwaZulu-Natal, Westville Campus, Durban 4000, South Africa.

**How to cite this paper:** Nakka Praveenkumar, Michael Hlongwane, Peter M. Norton, Wendy B. Mdlalose, Thishana Singh, Mathew K. Moodley. (2025) Mg-doped $Al_2O_3$ Nanoparticles: Synthesis, Structural, and Optical Studies Prepared Through Mechanical Ball Milling. *OAJRC Material Science*, 7(2), 24-33.
DOI: 10.26855/oajrcms.2025.12.001

**Received:** October 29, 2025
**Accepted:** November 30, 2025
**Published:** December 31, 2025

***Corresponding author:** Mathew K. Moodley, Discipline of Physics, University of KwaZulu-Natal, Westville Campus, Durban 4000, South Africa.

## Abstract

$Al_2O_3$ is a prominent material for high-temperature protective layers due to its exceptional chemical resistance, good oxidation resistance, and high-temperature stability. This work used a high-energy ball milling approach to synthesize pure $Al_2O_3$, $Al_{0.95}Mg_{0.05}O$, and $Al_{0.90}Mg_{0.10}O$ nanoparticles. After being heated to 1100°C, the pure $Al_2O_3$ and Mg-doped materials were examined for structural, morphological, elemental composition, and optical analyses. The pure γ-$Al_2O_3$ had a cubic structure at room temperature (RT), according to the X-ray diffraction (XRD) patterns, while the pure $Al_2O_3$ and Mg-doped samples showed a hexagonal crystal structure when heated to 1100°C. The crystallite size decreased from 37.85 nm to 32.32 nm with increasing Mg concentration in the Mg-doped samples, as indicated by the XRD patterns, which showed no impurities. The spherical form and aggregation of the synthesized $Al_2O_3$: Mg nanoparticles were shown by high-resolution transmission electron microscopy (HRTEM) images. The produced samples had an average particle size of 80.36 nm and 80 nm. The presence of magnesium in the $Al_2O_3$ lattice, as anticipated by the stoichiometric ratio, was confirmed by energy-dispersive X-ray spectroscopy (EDS). Moreover, the generated samples had no additional elements. UV-visible spectroscopy was used to measure the reflectance and optical band gap (Eg). The band gap energy dropped from 4.15 eV to 4 eV with increasing $Mg^{2+}$ concentrations.

## Keywords

Phase change; Mg-doped $Al_2O_3$; Ball milling technique; physical properties and 1100°C

## 1. Introduction

The high specific surface area, adsorption capability, and thermal stability of the host γ-$Al_2O_3$ powder make it an effective choice [1]. The stable rhombohedral α-alumina is one of the metastable phases of alumina (boehmite→ γ→δ→θ-$Al_2O_3$). Soft abrasives, phosphors, optical components, catalysts, and adsorbents are only a few of the commercial uses for γ-$Al_2O_3$ among these metastable phases [2]. Due to their low cost and optical properties, pure and doped alumina powder, as well as single crystals, have recently garnered significant scientific attention. Both (i) the methods for powder synthesis and (ii) the right dopants have been the subject of much investigation. The diffusion and variations in the interface energy may also have an impact on nanostability and the chemical composition of the surface. New developments in calorimetric methods for measuring nanoparticle interface energy have shown that surface energy varies as doping concentration rises.

Gamma alumina is one of the most important catalytic materials and is widely used as a catalyst or as a catalyst support [3]. Besides the properties of pristine γ-$Al_2O_3$, the use of dopants has been applied to improve its performance [4]. However, the acidity or basicity of the surface is thought to have a significant influence on the catalytic activity of doped or supported oxides. Michiko Kusunoki et al. [5] discussed the Mg-doped γ-$Al_2O_3$ fine particles prepared by evaporating metal Al in air. At 1400°C, particles are more stable, and the role of Mg atoms is. Raphael A.M.P. de Oliveira et al. [6] discussed the many applications, such as self-cleaning surfaces, photocatalytic activities, sensors, and sintering. Therefore, interface segregation-induced nanostability is a significant issue that has been partly ascribed to thermodynamic processes. Moreover, more investigations have been carried out in order to analyze the surface and physicochemical properties of aluminas in relation to their catalytic behaviour [7]. Industrial aluminas may be very impure when considering the composition of the crystal phase as well as the presence of contaminants. In particular, it is well-known that alkali metal impurities modify the acid-base properties and the reactivity of transitional aluminas [8-10].

The dopants are very important in altering the physical properties; several researchers investigated the Cr-doped γ-$Al_2O_3$ using the combustion technique [11], Eu-doped γ-$Al_2O_3$ prepared by the alkoxide sol–gel method [12], Cu-doped γ-$Al_2O_3$: A density functional theory study [1], Cr-doped γ- and α-$Al_2O_3$ synthesized via the Pechini route [13], and C-doped γ-$Al_2O_3$ powders produced by a modified polyacrylamide gel method [2]. The effects of impurities have been examined through various methods such as infrared (IR) spectroscopy [14, 15], X-ray photoelectron spectroscopy (XPS) [16], carbon dioxide adsorption followed by FT-IR and temperature-programmed desorption (TPD) [17], as well as simultaneous TPD and thermogravimetric (TG) analysis of alcohol [18].

In an $Al_2O_3$-based system, magnesium oxide (MgO) is a perfect reinforcing phase since it has excellent insulation and thermostability and can effectively make up for its lack of hydration reaction in air. Q. Gu et al. found that MgO films deposited on $Al_2O_3$ ceramic substrates would diffuse to form $MgAl_2O_4$ spinel at 700°C [19]. Ningkai Sun et al. [20] discussed that $Al_2O_3$ and MgO could react to form $MgAl_2O_4$ at a sintering temperature far below 1500 ◦C. The benefits of $MgAl_2O_4$ include a high melting point (2135 °C), resistance to chemical corrosion, and great mechanical qualities at both room temperature and elevated temperatures. Sakaguchi et al. [21] reported that Mg doping facilitates the homogenization of grain boundary diffusion in $Al_2O_3$.

In particular, the α-$Al_2O_3$ powder's superior heat conductivity and resistance, as well as its greater strength and hardness, make it very promising for a variety of applications, including sapphire crystal formation, electronics, semiconductors, and catalysts. In general, aluminium hydroxide at 500°C forms *γ*-alumina, which then transforms to *δ*-alumina and *θ*-alumina before becoming *α*-$Al_2O_3$ in the range of 1100°C [22]. The synthesis of α-$Al_2O_3$ is currently the subject of little investigation; nevertheless, it is more difficult to build a structure at a lower temperature due to the high formation temperature.

The goal of this study is to use the ball-milling process to create Mg-doped $Al_2O_3$ nanoparticles at weight percentages of 0, 5, and 10. The pure $Al_2O_3$ lattice and Mg-doped nanoparticles' structural, morphological, elemental, and optical characteristics were examined and documented.

## 2. Experimental Work

Mg-doped $Al_2O_3$ ($Al_{2-x}Mg_xO_3$, x=0.05, 0.10) powders with the Mg content of 5% and 10% were synthesized in a ball mill (Retsch, PM-400 MA-type), using a 250 ml stainless-steel jar with 10mm diameter zirconia balls. For the synthesis to be homogeneous and consistent in the creation of nanoparticles, careful mixing and mechanical grinding were required. The starting materials, $Al_2O_3$ (Alfa Aesar, 58 angstroms) and MgO (Sigma-Aldrich, -10-+50 mesh, 98%), were weighed based on the stoichiometric ratio and subsequently milled for 15 h in a room temperature atmosphere. With a powder-to-ball weight ratio of 1:3.44, 5 g of the powder mixture in total was ground. At a rotating velocity of 300 revolutions per minute (rpm), the milling operation was carried out. After milling, the pure $Al_2O_3$ and Mg-doped $Al_2O_3$ powders were each loaded into separate alumina crucibles and calcined in a high-temperature tube furnace (PT-1700T-50 (660)) at 1100°C for 10 hours in air. After heating samples, we thoroughly ground them using an agate mortar and pestle for 1.30 min. We focused on doped samples with different characterizations such as XRD, HRTEM, EDS, and UV-Vis-NIR studies.

### 2.1 Material characterization

Following the synthesis of the magnesium-doped $Al_2O_3$ nanoparticles, we closely investigated the following characterizations: the phase composition and powder crystal structure were investigated using X-ray diffraction (XRD, Rigaku mini flex, Kα rays). A UV-Vis-DRS (PerkinElmer Lambda 365+) spectrophotometer was used to measure the powder's reflectance spectrum, and high-resolution transmission electron microscopy (HRTEM, JSM-5600 LV) was used to examine its shape and elemental composition.

## 3. Results and Discussions

### 3.1 Phase and structural analysis

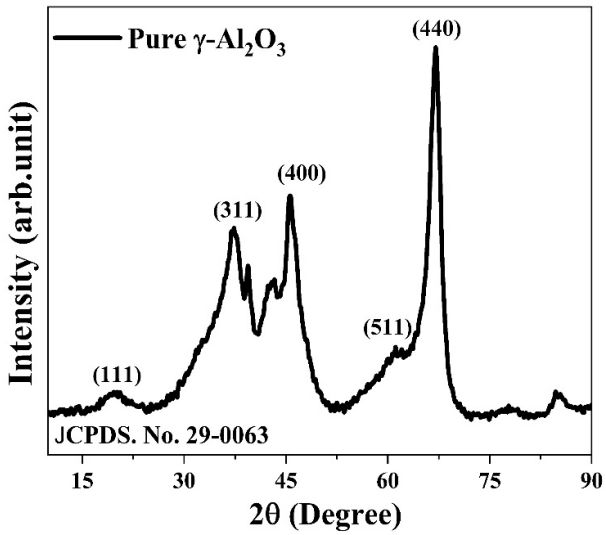


**Figure 1. X-ray diffraction pattern of γ-$Al_2O_3$ nanopowder at room temperature, showing characteristic peaks corresponding to the cubic phase.**

The XRD Patterns for undoped γ-$Al_2O_3$ nanopowder, in the 2θ scan range between 12°-90º, are shown in Figure 1. According to Figure 1, the 2θ and Miller indices values are 19.67°, 37.34°, 39.42°, 45.61°, 61.12°, and 67.03°, corresponding to hkl values of (111), (220), (311), (400), (511), and (440), respectively. We confirmed the γ-$Al_2O_3$ with a face-centered cubic crystal structure [2] and correlated it with JCPDS data [23].

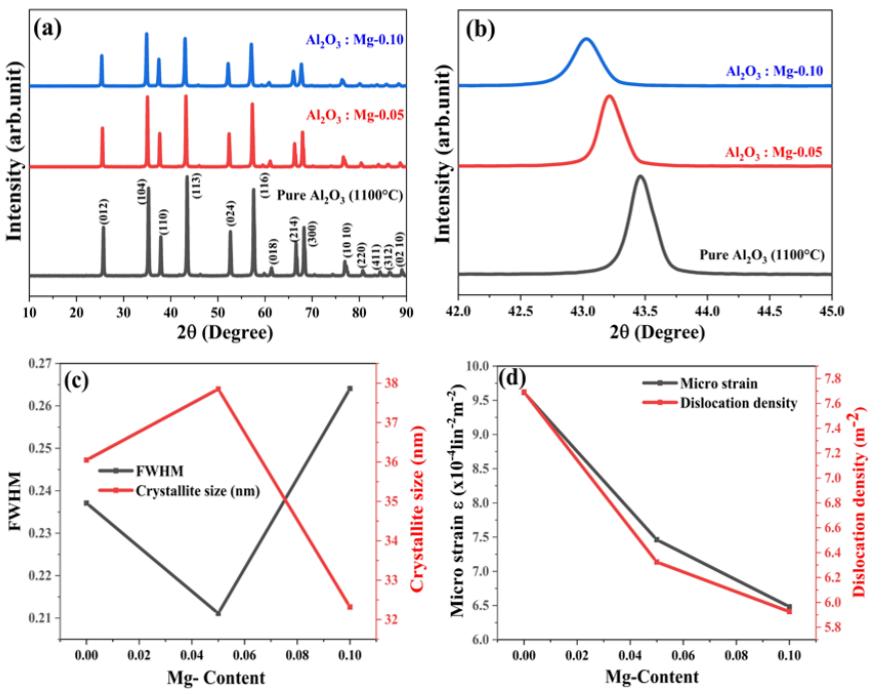


**Figure 2. (a) X-ray diffraction pattern of undoped $Al_2O_3$ (heated to 1100 °C) and Mg-doped $Al_2O_3$ nanoparticles, confirming the hexagonal α−$Al_2O_3$ phase; (b) Peak shift of the (113) reflection in the range 42°-45° due to Mg incorporation; (c) Variation of FWHM and crystallite size with Mg concentration; (d) Microstrain and dislocation density trends for pure and Mg-doped samples.**

Figure 2 (a) shows the pure $Al_2O_3$ at 1100°C and Mg-doped $Al_2O_3$ nanoparticles in the scan range 10°-90°. The 2θ angles and hkl values are 25.46° (012), 35° (104), 37.61° (110), 43.17° (113), 52.33° (024), 57.27° (116), 61.05° (018), 66.24° (214), 67.92° (300), 76.58° (10 10), 83.99° (220), 86° (312), 88.63° (02 10), respectively. For the Mg-doped nanoparticles, all the diffraction peaks are assigned to the α-$Al_2O_3$ phase and the hexagonal crystalline structure (JCPDS PDF No. 42-1468) [24]. No evidence of a crystalline phase or other peaks suggesting impurities was found in the Mg-doped $Al_2O_3$ system based on the diffraction patterns. Moreover, we noticed that all diffraction peaks are very sharp and fine, indicating that Mg-doped nanoparticles exhibited a good crystalline structure.

Figure 2 (b) shows the (113) diffraction peak shift in the scanned range between 42°-45° for pure $Al_2O_3$ (1100°C) and Mg-doped samples. The Mg entry into the $Al_2O_3$ matrix caused the peak to shift to the lower angle side, from 2θ = 43.44° to 43.03°, due to $Mg^{2+}$ having an ionic radius of 0.57 Å, which is very close to the ionic radius of $Al^{3+}$ (0.53 Å) [25, 26]. As the ionic radius of $Mg^{2+}$ and $Al^{3+}$, the dopant ion is larger than that of the pure system, indicating a difference of about 0.04Å. Prinston Melroy Lewis et al. [27] reported that the ionic radius difference for the dopant and pure lattice shifted to the lower angle side, and in the hexagonal crystal structure, the Al3+ ions occupy octahedral sites.

Figure 2 (c) shows the full-width half maximum (FWHM) and crystalline size of pure $Al_2O_3$ (1100°C) and Mg-doped samples. In the pure and Mg-doped samples, the crystallite size was determined using the Scherrer equation [28].

$$\text{Crystallite size (D)} = \frac{K\lambda}{\beta\cos\theta} \quad (1)$$

Where D is the crystallite size, *k* is a Scherrer constant, λ is the X-ray wavelength (1.5406Å), θ is the Bragg angle, and β is the full-width half maximum (FWHM). The pure γ-$Al_2O_3$ (in XRD pattern, 400 peak) has a crystallite size of 4.69 nm, and the average crystallite size is 3.402 nm. At 1100°C, the γ-$Al_2O_3$ phase changes to α-$Al_2O_3$ [22]. For pure $Al_2O_3$ (1100° C) and Mg-doped samples, the crystallite sizes are 36.05 nm, 37.85 nm, and 32.32 nm, respectively. The crystallite size decreases as the Mg content increases, which indicates the increased grain boundaries in Mg-doped $Al_2O_3$ nanoparticles and segregates to the boundaries. Adnan A. Mohammed et al. [29] discussed a similar crystallite size by using the Scherrer relation. The average crystallite size of pure $Al_2O_3$ (1100°C), Mg-doped samples is 30.60 nm, 33.55 nm, and 25.66 nm, respectively.

Figure 2 (d) shows the micro strain and dislocation density of pure (at 1100°C) and Mg-doped samples. The two parameters are indicators of crystal defects, and we measured the pure and doped samples by using the mathematical equation [28].

$$\text{Micro-strain } (\varepsilon) = \frac{\beta\cos\theta}{4} \quad (2)$$

$$\text{Dislocation density } (\delta) = \frac{1}{D^2} \quad (3)$$

Where β is the full-width half maximum (FWHM), θ is the Bragg angle, and D is the average crystallite size. The comparison of pure $Al_2O_3$ (1100°C) and doped samples shows that microstrain and dislocation density decrease with Mg content. When magnesium ($Mg^{2+}$) was doped to the $Al_2O_3$ lattice, there was a discernible drop in microstrain and dislocation density. This was because the dopant stabilised the crystal structure and reduced the production of imperfections during synthesis. Table 1 describes the XRD parameters of pure and Mg-doped samples.

**Table 1. X-ray diffraction parameters of pure $Al_2O_3$ and Mg-doped samples**

| System Name | 2θ (degree) | FWHM | Crystallite size D (nm) | Micro strain ($10^{-4}$) | Dislocation density ($10^{14}$) $m^{-2}$ |
|---|---|---|---|---|---|
| γ-$Al_2O_3$ | 67.03 | 2.0296 | 4.69 | 73.83 | 453.714 |
| Pure $Al_2O_3$ (1100°C) | 43.44 | 0.2371 | 36.05 | 9.614 | 7.692 |
| Mg-0.05 | 43.21 | 0.2111 | 37.85 | 7.462 | 6.325 |
| Mg-0.10 | 43.03 | 0.2641 | 32.32 | 6.483 | 5.926 |

### 3.2 Surface morphology studies

The surface morphology of the Mg-doped $Al_2O_3$ nanoparticles was studied using High-Resolution Transmission Electron Microscopy (HRTEM), as shown in Figure 3. At Mg content of 0.05, the particles are spherical and agglomerated in the range of 200 nm, as shown in Figure 3 (a). Moreover, the non-uniformity in size distribution has been observed. In the range of 5 nm, the d value 0.964 nm was confirmed, and the average particle size was estimated as 80.36 nm by using a histogram plot, as shown in Figure 3 (b and c). Based on Figure 3 (d, e, and f), at Mg (x=0.10), the particles are close to each other, irregular in shape, and are agglomerated. The average particle size is 81.00 nm, and the d values are 0.203 nm and 0.243 nm. The comparison of lower and higher concentrations, particles are very close to each other compared to the lower concentration (Mg-0.05), and a small change in particle size is observed with varying dopant concentration. Lingling Zhu et al. [30] discussed the low-temperature synthesis of polyhedral α-$Al_2O_3$ nanoparticles through ball milling, aggregation of the transition phase alumina at 800 °C and 900 °C. In other words, only when the transition phase particle size was greater than 30 nm did the phase transition occur [31]. P. Billik et al. [32] discussed 1000°C; the newly formed aggregates consisting of the α-$Al_2O_3$ phase have a vermicular morphology. V. Udhayabanu et al. [33] discussed that at 1150°C, the TEM bright field image of α-$Al_2O_3$ reveals its nanocrystalline nature with the average crystallite size of 100 nm.

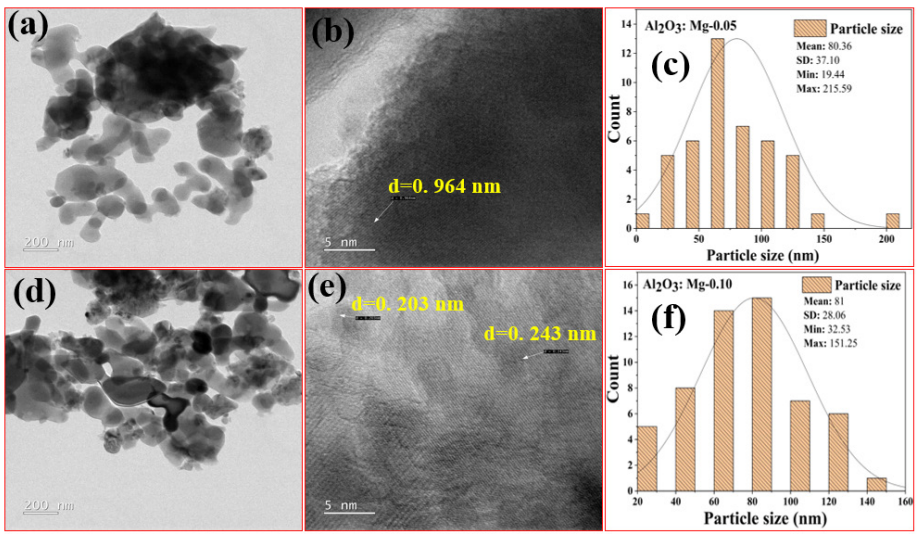


**Figure 3. High-resolution transmission electron microscopy (HRTEM) images and particle size distribution of Mg-doped $Al_2O_3$ nanoparticles: (a-c) $Mg_{0.05}$ sample showing spherical morphology and agglomeration; (d-f) $Mg_{0.10}$ sample exhibiting irregular shapes and closer particle clustering.**

### 3.3 Chemical composition studies

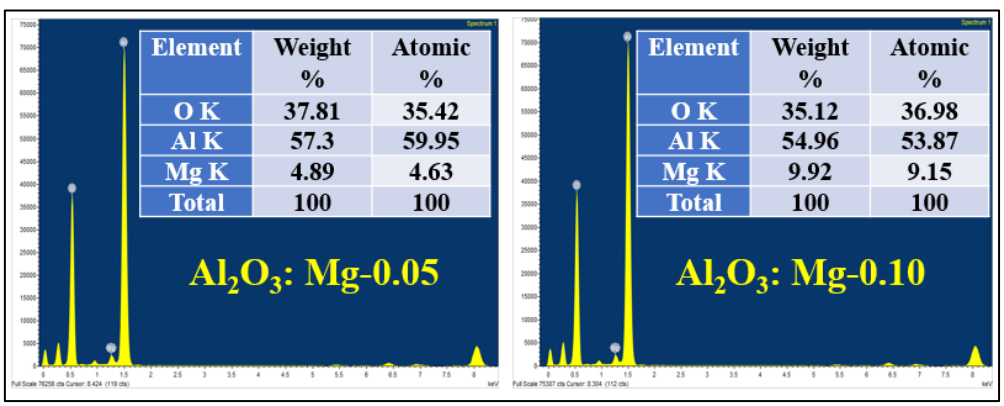


**Figure 4. EDX spectra of Mg-doped $Al_2O_3$ nanoparticles.**

Figure 4 shows the elemental composition of Mg-doped (x=0.05 and 0.10) $Al_2O_3$ nanoparticles. The figure indicates the expected elements are involved in the $Al_2O_3$ system, such as Al, O, and Mg. The other impurities are not involved, and the nearly expected percentage of both confirmed concentrations. These results are confirmed by XRD and the purity of Mg-doped nanoparticles.

### 3.4 Optical properties

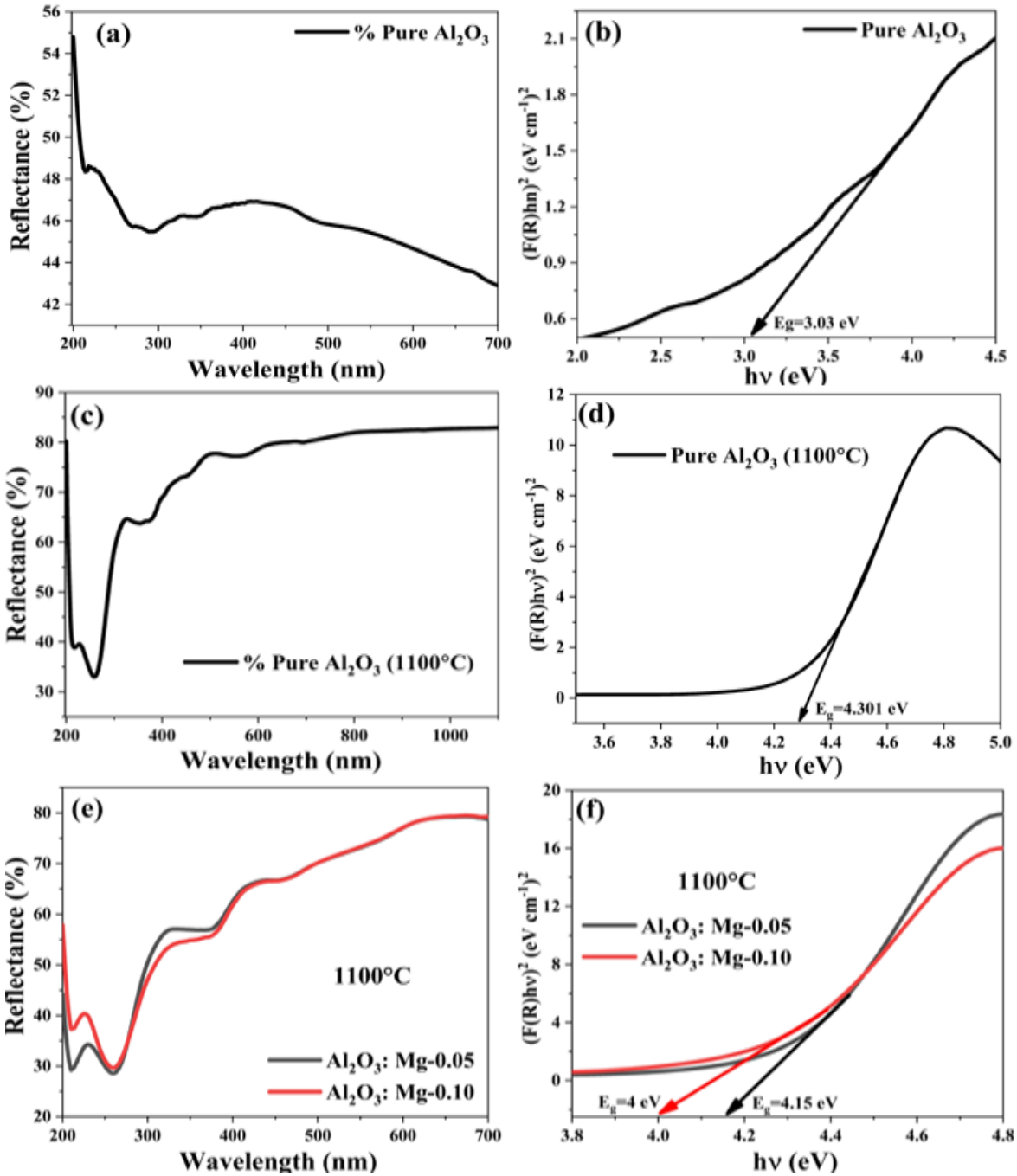


**Figure 5. Diffused reflectance spectroscopy (DRS) and optical band gap (Eg) analysis: (a) DRS of γ-$Al_2O_3$; (b) Eg of γ-$Al_2O_3$; (c) DRS of pure $Al_2O_3$ at 1100 °C; (d) Eg of pure $Al_2O_3$; (e) DRS of Mg-doped $Al_2O_3$; (f) Eg of Mg-doped $Al_2O_3$, illustrating band gap reduction with increasing Mg concentration.**

The reflectance of pure γ-$Al_2O_3$ as shown in Figure 5 (a), the maximum reflectance (55%) was seen. The optical band gap (Eg) is 3.03 eV for pure γ-$Al_2O_3$, as shown in Figure 5 (b). The theoretical formation energy for one oxygen vacancy in $Al_2O_3$ is reported within a wide range of 1.32-7.08 eV [34] to 10-16.38 eV [35, 36]. Kaveh Edalati et al. [37] reported the optical band gap of γ-$Al_2O_3$, below 3 eV. In this study, based on first-principles calculations, the $Al_2O_3$ bandgap can be reduced to 2.5 eV with large oxygen vacancy concentrations via the high-pressure torsion (HPT) method. Oxygen vacancies on bandgap narrowing of $Al_2O_3$ [38].

Figure 5 (c) shows the DRS of pure $Al_2O_3$ (1100°C), in the wavelength range of 200 nm-1100 nm. The highest reflectance was seen at the visible range 400-800 nm. The optical band gap of pure $Al_2O_3$ (1100°C) is 4.301 eV. To analyze the effect of Mg concentration on the optical properties of the $Al_2O_3$ system. Figure 5 (e) shows the UV-Vis-reflectance spectra with a scanned wavelength range between 200 and 700 nm. According to the reflectance spectra, a 200 to 400 nm variation was observed, but in the 400 to 800 nm there is no variation and was close to each other. The highest reflectance was seen in the visible range (400-700 nm), and the lowest reflectance spectra were in the ultraviolet region (200-400 nm). Moreover, Figure 5 (f) shows the optical band gap of the Mg-doped $Al_2O_3$ system, in photon energy (hν), in the range between 3.8 eV and 4.8 eV. To determine the optical band gap of pure and doped samples by using the Kubelka-Munk function F(R) [39] and the Tauc equation [40].

$$F(R) = \frac{(1-R)^2}{2R} \tag{4}$$

$$F(R).h\nu = A(h\nu - E_g)^n \tag{5}$$

Where the absorption coefficient is denoted by F (R)=α, the reflectance by R, the photon energy by hν, the constant A, the Planck constant by h, the energy of the optical band gap between the valence and conduction bands by Eg, and the transition type by n (n=1/2: directly allowed, 2: indirectly allowed, 3/2: directly prohibited, and 3: indirectly forbidden). In the present case, n was taken ½ directly allowed transition. The Eg of the samples was obtained by extrapolating the linear region to α= 0, the graph plotted between $(F(R)h\nu)^n$ and hν.

The Eg values of x=0.05, 0.10 are 4.15 and 4 eV, respectively. The optical band gap values decreased with increasing Mg concentration. The decreasing band gap may affect certain parameters, such as dopant, lattice defects, and particle size, among others. Majid Farahmandjou et al. [40] reported that the band gap decreases due to the charge transfer between the $Mg^{2+}$ ions and the valence or conduction band ions of $Al_2O_3$. Moreover, the sol–gel synthesis of Ce-doped α-$Al_2O_3$, a similar decrease in band gap of 2% (3.57 eV), 4 % (3.40 eV), and 6% (3.29 eV), respectively. Abolfazl Khodadadi et al. [41] discussed how the optical band gap decreases, as this impurity band prevents the recombination of electron-hole pairs and causes the separation of the electron-hole. This impurity band hybridized with the $O_2$ network defects' energy band, and by creating an impurity band, it stopped the alumina conduction band from trapping holes, resulting in a drop in the energy band. Sm and Co-doped $Al_2O_3$ system via ball-milled process using 1000°C, a similar band gap was seen [42].

## 4. Conclusion

In summary, the $Al_{0.95}Mg_{0.05}O$ and $Al_{0.90}Mg_{0.10}O$ samples were successfully synthesized using the ball milling method. The X-ray diffraction study confirmed that the pure γ-$Al_2O_3$ phase has a cubic structure. The α-$Al_2O_3$ phase at 1100 °C and Mg-doped samples α-$Al_2O_3$ phase is a hexagonal crystal structure with high crystallinity. Furthermore, from the patterns, $Mg^{2+}$ ions properly settled in the $Al_2O_3$ lattice, and microstrain (9.614-6.483) and dislocation density (7.692-5.926) decreased with the increase in Mg concentrations. Based on morphological and elemental composition studies, it was confirmed that the particles are spherical and their diameter changed with Mg content. Agglomeration clearly increased with high Mg (0.10%) concentration, and the elements involved were Al, O, and Mg. The elemental composition clearly states that no other elements are present, the purity of $Al_2O_3$: Mg, and the expected stoichiometric ratio of doped samples. The optical studies confirmed that the optical band gap decreased from 4.15 eV to 4 eV. Finally, the physical properties of $Al_2O_3$ are purely dependent on the temperature and the doping effect. These results are useful for the understanding of the stable phase and $Mg^{2+}$ ions.

## CRediT authorship contribution statement

Mathew K. Moodley and Wendy B. Mdlalose: Conceptualization. Nakka Praveenkumar: Investigation, Data curation, Writing – original draft. Michael Hlongwane: Investigation, Data curation. Peter M. Norton and Wendy B. Mdlalose: Investigation. Mathew K. Moodley, Thishana Singh, and Wendy B. Mdlalose: Supervision, Methodology, Writing – review & editing.

## Declaration of Competing Interest

The authors declare that they have no known competing financial interests or personal relationships that could have appeared to influence the work reported in this paper.

## Data availability

The datasets generated during and/or analysed during the current study are available from the corresponding author on reasonable request.

## Acknowledgement

MKM and NP thank the College of Agriculture, Science and Engineering, University of KwaZulu-Natal, for the postdoctoral fellowship. TS thanks the National Research Foundation South Africa for a Competitive Programme for Rated Researchers grant [CPRR230527110705]. WBM the National Research Foundation, South Africa for a Thuthuka Postdoctoral track [TTK23041392505]. The authors acknowledge the University of KwaZulu-Natal for the generous use of the equipment for the following analyses: XRD, HRTEM, and UV-vis-NIR analysis.

## References

[1] Liu S, Huang Y, Lu Z, Cen W, Yu X, Qing S, et al. Surface property of the Cu doped γ-Al2O3: A density functional theory study. Appl Surf Sci. 2021;535:147651. doi:10.1016/j.apsusc.2020.147651.

[2] Wang SF, Zhuang CF, Yuan YG, Xiang X, Sun GZ, Ding QP, et al. Synthesis and Photoluminescence of γ-Al2O3 and C-doped γ-Al2O3 Powders. Trans Indian Ceram Soc. 2014;73(1):37-42. doi:10.1080/0371750X.2014.890464.

[3] Cai W, Zhang S, Lv J, Chen J, Yang J, Wang Y, et al. Nanotubular gamma alumina with high-energy external surfaces: synthesis and high performance for catalysis. ACS Catal. 2017;7(6):4083-92. doi:10.1021/acscatal.7b00080.

[4] Keyvanloo K, Mardkhe MK, Alam TM, Bartholomew CH, Woodfield BF, Hecker WC. Supported iron Fischer-Tropsch catalyst: Superior activity and stability using a thermally stable silica-doped alumina support. ACS Catal. 2014;4(4):1071-7. doi:10.1021/cs401242d.

[5] Kusunoki M, Rokkaku M, Ikuhara Y, Yanagida H. TEM study on stability of Mg-doped γ-alumina fine particles. Mater Trans JIM. 1998;39(1):110-3. doi:10.2320/matertrans1989.39.110.

[6] de Oliveira RAMP, da Silva AL, Caliman LB, Gouvêa D. Interface excess on Li2O-doped γ-Al2O3 nanoparticles. Ceram Int. 2020;46(8 Pt B):10555-60. doi:10.1016/j.ceramint.2020.01.057.

[7] Lambert JF, Che M. The molecular approach to supported catalysts synthesis: state of the art and future challenges. J Mol Catal A Chem. 2000;162(1-2):5-18. doi:10.1016/S1381-1169(00)00318-6.

[8] Pines H, Haag WO. Alumina: catalyst and support. I. alumina, its intrinsic acidity and catalytic activity. J Am Chem Soc. 1960;82(10):2471-83. doi:10.1021/ja01495a021.

[9] Hall WK, Lutinski FE, Gerberich HR. Studies of the hydrogen held by solids: VI. The hydroxyl groups of alumina and silica-alumina as catalytic sites. J Catal. 1964;3:512-27. doi:10.1016/0021-9517(64)90051-X.

[10] Busca G. The surface of transitional aluminas: A critical review. Catal Today. 2014;226:2-13. doi:10.1016/j.cattod.2013.08.003.

[11] Kakooei S, Rouhi J, Mohammadpour E, Alimanesh M, Dehzangi A. Synthesis and characterization of Cr-doped Al2O3 nanoparticles prepared via aqueous combustion method. Casp J Appl Sci Res. 2012;13:16-22.

[12] Wrzyszcz J, Miśta W, Hreniak D, Stręk W, Zawadzki M, Grabowska H. Preparation and optical properties of nanostructured europium-doped γ-Al2O3. J Alloys Compd. 2002;341(1-2):358-61. doi:10.1016/S0925-8388(02)00037-3.

[13] Salek G, Devoti A, Lataste E, Demourgues A, Garcia A, Jubera V, et al. Optical properties versus temperature of Cr-doped γ-and α-Al2O3: Irreversible thermal sensors application. J Lumin. 2016;179:189-96. doi:10.1016/j.jlumin.2016.07.004.

[14] Mohammed Saad AB, Ivanov VA, Lavalley JC, Nortier P, Luck F. Comparative study of the effects of sodium impurity and amorphisation on the Lewis acidity of γ-alumina. Appl Catal A Gen. 1993;94(1):71-83. doi:10.1016/0926-860X(93)80046-S.

[15] Srinivasan S, Narayanan CR, Datye AK. The role of sodium and structure on the catalytic behavior of alumina: II. IR spectroscopy. Appl Catal A Gen. 1995;132(2):289-308. doi:10.1016/0926-860X(95)00162-X.

[16] Scokart PO, Amin A, Defossa C, Rouxhet PG. Direct probing of the surface properties of alkali-treated aluminas by infrared and x-ray

photoelectron spectroscopy. J Phys Chem. 1981;85(10):1406-12. doi:10.1021/j150610a027.

[17] Ivanov VA, Piéplu A, Lavalley JC, Nortier P. Effect of sodium oxide on the morphology and basicity of alumina. Appl Catal A Gen. 1995;131(2):323-34. doi:10.1016/0926-860X(95)00149-2.

[18] Srinivasan S, Narayanan CR, Biaglow A, Gorte R, Datye AK. The role of sodium and structure on the catalytic behavior of alumina: I. Isopropanol dehydration activity. Appl Catal A Gen. 1995;132(2):271-87. doi:10.1016/0926-860X(95)00161-1.

[19] Gu Q, Zhang YX, Ma WK, Liu GQ, Liu XH, Li HX. Interfacial spinellisation of MgO-C/Al2O3-C composite functional refractory component at high temperatures. Ceram Int. 2021;47(2):2705-14. doi:10.1016/j.ceramint.2020.09.122.

[20] Sun N, Jiang H, Zhao X, Deng X, Zhang W. High-temperature protection performance of Mg-doped Al2O3 protective layers on the thin film thermocouples. Ceram Int. 2024;50(20 Pt B):36537-43. doi:10.1016/j.ceramint.2024.07.040.

[21] Sakaguchi I, Srikanth V, Ikegami T, Haneda H. Grain-boundary diffusion of oxygen in alumina ceramics. J Am Ceram Soc. 1995;78(9):2557-9. doi:10.1111/j.1151-2916.1995.tb08703.x.

[22] Kim HS, Park NK, Lee TJ, Um MH, Kang M. Preparation of Nanosized α‐Al2O3 Particles Using a Microwave Pretreatment at Mild Temperature. Adv Mater Sci Eng. 2012;2012:920105. doi:10.1155/2012/920105.

[23] Buwono HP, Adiwidodo S, Wicaksono H, Firmansyah HI. Hydrothermal synthesis and characterization of nano-particles γ-Al2O3. IOP Conf Ser Mater Sci Eng. 2021;1073(1):012011. doi:10.1088/1757-899X/1073/1/012011.

[24] Rani G, Sahare PD. Structural and photoluminescent properties of Al2O3: Cr3+ nanoparticles via solution combustion synthesis method. Adv Powder Technol. 2014;25(2):767-72. doi:10.1016/j.apt.2013.11.009.

[25] Kılınç N, Arda L, Öztürk S, Öztürk ZZ. Structure and electrical properties of Mg‐doped ZnO nanoparticles. Cryst Res Technol. 2010;45(5):529-38. doi:10.1002/crat.200900662.

[26] Heiba ZK, Mohamed MB, Wahba AM, Imam NG. Structural, optical, and electronic characterization of Fe-doped alumina nanoparticles. J Electron Mater. 2018;47(2):711-20. doi:10.1007/s11664-017-5830-0.

[27] Lewis PM, Keerthana N, Hebbar ND, Choudhari KS, Kulkarni SD. Cr3+ doped Al2O3 nanoparticles: Effect of Cr3+ content in intensifying red emission. Curr Appl Phys. 2021;32:71-7. doi:10.1016/j.cap.2021.10.003.

[28] Praveenkumar N, Rao NM. Ni doped Zn3P2 nanoparticles: synthesis, structural, optical, and magnetic properties. J Supercond Nov Magn. 2023;(article in press). doi:10.1007/s10948-023-06670-w.

[29] Mohammed AA, Khodair ZT, Khadom AA. Preparation and investigation of the structural properties of α-Al2O3 nanoparticles using the sol-gel method. Chem Data Collect. 2020;29:100531. doi:10.1016/j.cdc.2020.100531.

[30] Zhu L, Liu L, Sun C, Zhang X, Zhang L, Gao Z, et al. Low temperature synthesis of polyhedral α-Al2O3 nanoparticles through two different modes of planetary ball milling. Ceram Int. 2020;46(17):28414-21. doi:10.1016/j.ceramint.2020.07.346.

[31] Morinaga K, Torikai T, Nakagawa K, Fujino S. Fabrication of fine α-alumina powders by thermal decomposition of ammonium aluminium carbonate hydroxide (AACH). Acta Mater. 2000;48(18-19):4735-41. doi:10.1016/S1359-6454(00)00265-2.

[32] Billik P, Čaplovičová M, Turányi T, Čaplovič L, Horváth B. Low-temperature mechanochemical–thermal synthesis of α-Al2O3 nanocrystals. Mater Res Bull. 2011;46(11):2135-40. doi:10.1016/j.materresbull.2011.06.022.

[33] Udhayabanu V, Murty BS. Synthesis of Nanocrystalline α-Al2O3 from Nanocrystalline Boehmite Derived from High Energy Ball Milling of Gibbiste. Trans Indian Inst Met. 2011;64(4-5):535-40. doi:10.1007/s12666-011-0086-5.

[34] Tanaka I, Oba F, Tatsumi K, Kunisu M, Nakano M, Adachi H. Theoretical formation energy of oxygen-vacancies in oxides. Mater Trans. 2002;43(7):1426-9. doi:10.2320/matertrans.43.1426.

[35] Carrasco J, Gomes JRB, Illas F. Theoretical study of bulk and surface oxygen and aluminum vacancies in α-Al2O3. Phys Rev B. 2004;69(6):064116. doi:10.1103/PhysRevB.69.064116.

[36] Janetzko F, Evarestov RA, Bredow T, Jug K. First‐principles periodic and semiempirical cyclic cluster calculations for single oxygen vacancies in crystalline Al2O3. Phys Status Solidi B Basic Res. 2004;241(5):1032-40. doi:10.1002/pssb.200301961.

[37] Edalati K, Fujita I, Takechi S, Nakashima Y, Kumano K, Razavi-Khosroshahi H, et al. Photocatalytic activity of aluminum oxide by oxygen vacancy generation using high-pressure torsion straining. Scr Mater. 2019;173:120-4. doi:10.1016/j.scriptamat.2019.08.011.

[38] Choi M, Janotti A, Van de Walle CG. Native point defects and dangling bonds in α-Al2O3. J Appl Phys. 2013;113(4):044501. doi:10.1063/1.4784114.

[39] Lacombe S, Cardy H, Soggiu N, Blanc S, Habib-Jiwan JL, Soumillion JP. Diffuse reflectance UV–Visible spectroscopy for the qualitative and quantitative study of chromophores adsorbed or grafted on silica. Microporous Mesoporous Mater. 2001;46(2):311-9. doi:10.1016/S1387-1811(01)00315-8.

[40] Farahmandjou M, Motaghi S. Sol–gel synthesis of Ce-doped α-Al2O3: study of crystal and optoelectronic properties. Opt Commun. 2019;441:1-7. doi:10.1016/j.optcom.2019.02.029.

[41] Khodadadi A, Farahmandjou M, Yaghoubi M. Investigation on synthesis and characterization of Fe-doped Al2O3 nanocrystals by new sol–gel precursors. Mater Res Express. 2018;6(2):025029. doi:10.1088/2053-1591/aaef70.

[42] Wahab H, Khan RTA, Iqbal M. Tuning the local structure of (Sm, Co) Co-doped Al2O3 system for optical band gap and low dielectric loss. Ceram Int. 2024;50(23 Pt B):49235-42. doi:10.1016/j.ceramint.2024.09.267.